Metamachines of Pluripotent Colloids

Antoine Aubret, Quentin Martinet, Jeremie Palacci

Metamachines of Pluripotent Colloids

Antoine Aubret,[1,2*] Quentin Martinet,[1] Jeremie Palacci[1*]

[1]Department of Physics, University of California San Diego

[2]Current Address: Univ. Bordeaux, CNRS, LOMA, UMR 5798, F-33405 Talence, France

Machines are assemblages of parts that transmit forces, motion, and energy one to another in a predetermined manner. Their development, the thermal engine as a prototypical example, thrusted the industrial revolution and modern technological progress. Engineering micromachines with encoded dynamics is broadly sought-after but challenging, requiring energy injection and faithful assembly at the microscale. Realizations are scarce with use of macroscopic fields[1,2] or concerted behavior of internally-driven parts[3–9] to power monolithic templates[2,6–8,10], with limited modularity. Progress in colloidal design now allows one to control assembly and shows potential to engineer dynamical micromachines. Resulting structures to date[11–15] are however in equilibrium and static, programmed into passive colloids that lack the ability to exert forces or reprogram autonomously. Here we show the design and assembly of functional and reconfigurable metamachines, or machines made of machines, from active colloids and optical templates. The architectures are autonomous, mobile and remain stable after removal of holographic traps[16] initially shaping the structure. Our strategy relies on non-equilibrium features of colloidal heterodimers, that couple self-propulsion and force generation with orientation in a light field. We rationalize our observations using analytical and numerical calculations of the optical field and a classification of the heterodimers of the structure by a function set by their local environment. Particles in the core exert attractive interactions and maintain cohesion, while particles at the edge exert forces, and prescribe the dynamics of the micromachines. Active particles reprogram au-

tonomously following changes in local arrangement making possible to devise reconfigurable machines and complex architectures by template-and-merge of substructures. We notably demonstrate the design of ~ 40 colloidal architectures, with specified dynamics. We anticipate our approach will inspire the engineering of more sophisticated metamachines and shift the focus of self-assembly towards active matter and reprogrammable materials.

The potential of mobile micromachines to probe and manipulate matter at small scales makes them a sought-after goal and a challenge for applied and basic science[17]. Their engineering however departs from mere scale reduction of macroscopic robots[18,19] and encounters the challenges of assembly and reconfigurability at small scale. Functional micromachines prominently uses monolithic templates to position active agents[20–24] and encode function: microswimmers power micrometric gears[6–8], or dynamical micromachines assemble and move by field-induced interactions[2]. Rigid templates however come with limited reprogrammability. Light templates present spatio-temporal control with sub-micron resolution that can overcome this limitation as recently highlighted by the painting of light-powered strains of motile *E. Coli*[25,26]. While optical tweezers are the workhorse of particles' manipulation at the microscale[16], the tedious pick-and-place of all components, and permanent binding requirements plagued their use for the assembly of structures. Here we demonstrate, the design and assembly of multi-functional and reconfigurable *metamachines* from active colloids. The architectures are autonomous, mobile and stable after shape- initiation by a template of optical traps. It is made possible by harnessing the non-equilibrium properties of active particles to maintain the stability of templated architecture and achieve specified dynamics. We take advantage of the chemical and physical anisotropy of colloidal heterodimers [Fig.1A], leading to their self-propulsion and orientation in an optical field, to control anisotropic and reprogrammable interactions between particles. Our approach overcomes traditional limitations of optical tweezers for their use in self-assembly and engineering of micromachines.

Patterns of optical traps are placed in close-packed arrangements occupied by active het-

erodimers to form metamachines, that move autonomously [Fig.1B]. The heterodimers composing the structure are physically identical but differ in their orientations as a result of their number of nearest neighbors, producing different effective interactions and forces and displaying different functions. Particles in the core sit vertically and exert attractive forces maintaining the cohesion of the structure; particles at the boundary lay flat on the substrate exerting forces that prescribe the dynamics of the structure. Following reorganization in the structure, particles reorient reversibly. It follows that particles reprogram autonomously making possible the reconfiguration and assembly of machines by merging sub-structures. They reorganize internally to exhibit specified dynamics dictated by changes of templates [movie S1]. We demonstrate the design of over 40 metamachines [Fig.1C-F, movies S3-S5, Extended Fig.1], whose dynamics we rationalize.

Activity-assisted Optical Trapping. We devise colloidal heterodimers [Fig.1A] that couple anisotropic optical and chemical response. They are made of a polymeric bead of 3-(Trimethoxysilyl)propyl methacrylate (TPM, radius $R_T \approx 0.6$ μm) bound to a hematite particle (α-Fe_2O_3, radius $R_H \approx 0.3$ μm). Dieletric TPM has a real index of refraction in the visible range, $n_{TPM} = 1.51$, and is chemically inert, while hematite is both absorbing and photocatalytic. The heterodimers are based on synthesis previously reported[28] with chemical modifications improving the stability of heterobonds to prolonged light exposure [Materials and Methods]. Experiments are performed on a custom-made microscope, allowing superimposition of spatially-uniform blue light controlling the photocatalytic activation of hematite[27] ($\lambda = 425 - 500nm$), with patterns of holographic traps[29] controlled by a spatial light modulator (SLM) and a red laser at $\lambda_r = 639$ nm (waist $w_0 = 420nm$ and incident power $P = 0.1 - 1$ mW), a wavelength at which hematite has high extinction cross-section and negligible photocatalytic activity [Materials and Methods].

The heterodimers transduce energy from chemical gradients into motion[30] and self-propel under blue illumination[9,27] in aqueous solutions of hydrogen peroxide, $H_2O_2 \sim 6\%$wt. A dilute

suspension of those particles is introduced in a sealed glass capillary and sediments to a surface fraction $\sim 0.1\%$. Following activation, they propel along the substrate with the polymer part leading, and perform a persistent random walk[20,31] with speed $v_s \approx 15$ μm/s and persistence time $\tau_r \approx 1$s. It leads to effective diffusion for times, $t \gg \tau_r$ with diffusivity $D_{eff} = v_s^2 \tau_r/2 \sim 110 \mu m^2/s$ [Material and Methods].

The dynamic is drastically modified when an active heterodimer crosses an optical trap: the particle swiftly reorients and aligns along the optical axis of the incident red light, the polymer spheres lying on the surface as the hematite sits on top, making possible to immobilize particles according to a pattern [Fig.2A]. In equilibrium, *i.e.* absence of photocatalytic activity or H_2O_2 fuel, strong scattering forces on the hematite lead to the expulsion of the heterodimer from any region of high red intensity. We measure the lifetime τ of an heterodimer in an optical trap at fixed propulsion speed v_s and observe its increase with increased trap strength [Fig.2B] with stable trapping, $\tau > 100$ s for an incident power $P = 0.5$ mW, or a trap stiffness $\kappa \approx 0.8$ pN/μm obtained by conventional calibration with TPM beads [Supplementary Information].

Remarkably, the restoring force from the optical trap, $\sim \kappa w_0/2$, compares with the effective propulsive force $\gamma v_s \approx 0.1 - 0.2$ pN of the heterodimer, γ being the Stokes' drag, thus indicative of a balance between optical forces and self-propulsion. The reorientation of the heterodimer in a trap results from the momentum transfer between the incoming red light and the particle, set by the geometry and optical properties of the heterodimer as well as structure of the incident beam. Optical forces on the dielectric TPM component are dominated by gradient forces, as in conventional optical trapping, with a restoring force towards the center of the trap. Hematite, however, primarily experiences upward scattering forces in addition to gradient forces, due to its complex refractive index[32]. In effect, it leads to out-of-focus repulsion of the hematite and reorientation of the heterodimer by a torque $M_{scat}(\theta)$ [Fig.2C]. Following reorientation, particles

propel against the radiation pressure, and stable trapping originates in propulsive forces larger than optical repulsion, leading to particles pushing against the substrate.

To quantitatively describe the phenomenon, we perform analytic calculations[33] and 3D simulations using finite elements method (Comsol). We estimate the optical forces[32] acting on the particle at different heights and distances from an incident focused beam in water, with waist $w_0 \approx 400$ nm [Fig.2D-E and Materials and Methods]. We evaluate numerically the optical torque $M_{scat}(\theta)$ for different laser power P measured in the experiment, thus confirming that increased laser power results in larger aligning optical torques [Fig.2D]. In the experiment, we further observe that heterodimers propel on the substrate with a slant, $\theta \approx -\pi/8$ rad, as a result of phoretic and hydrodynamic interactions of the particles with their mirror-image with no-slip boundary conditions[34,35]. The resulting torque $M_S(\theta)$ is quantified from the experimental distribution of swimmers' orientation measured by simultaneous tracking of the hematite and TPM component [SI]. The comparison between $M_S(\theta)$ and $M_{scat}(\theta)$ reveals comparable magnitude in a range of accessible incident power [Fig.2D] and requires the inclusion of torque $M_S(\theta)$ to perform quantitative predictions. The interplay between particles propulsion and optical forces leads to their crossing, trapping or expulsion by an optical trap. We simulate the trajectories of non-brownian heterodimers reaching the laser spot by incorporating propulsive and drag forces as well as M_{scat} and M_S torques. We summarize the predicted behavior on a phase diagram $\{P, V_S\}$, where stable trapping is defined by steady position of a particle within the region defined by the waist and the Rayleigh range of the incident light [Fig.2E, Materials and Methods]. The quantitative agreement between the predicted phase diagram and the experiments confirms the proposed scenario for the trapping of active heterodimers [Fig.2E].

Remarkably, the enhanced diffusion of the self-propelled particles, $D_{eff} \sim 110$ μm^2, 200-fold the diffusivity of identical microparticles in equilibrium, guarantees the rapid occupancy of

static traps even using dilute suspensions of active particles. It takes typically $\mathcal{A}/4D_{eff} \sim 24$s for self-propelled particles to occupy optical traps distributed over an area $\mathcal{A} \sim 10^4 \mu m^2$ [Fig.2A, movie S2], thus overcoming traditional limitations of optical manipulation of micrometric objects, thermally too slow to explore the energy landscape set by the optical traps. The non-equilibrium nature of the active heterodimers is two-fold: it allows the rapid positioning of self-propelled particles in static optical traps and effective interactions resulting from the coupling between particles' orientation and propulsive forces. It opens opportunities for assembly that we explore below.

Assembly of Dynamical and Reconfigurable Metamachines. As the optical traps are removed, particles initially captured in distant traps self-propel randomly and the template vanishes. In contrast, the initial structure remains stable for particles organized in close-packed arrangements and exceeding two neighbors. Particles, which all stood vertically in the traps, evolve differentially depending on local arrangement after removal of the optical traps [Fig.3A]. Heterodimers surrounded by 5 or 6 nearest neighbors remain vertical, as a result of neighbors' excluded volume interactions. Facing the substrate, they generate an attractive flow[36,37], providing cohesion to the machine. Heterodimers with 3 or 4 neighbors evolve to lay flat on the substrate [Fig.3A]. They exert forces on the structure directed along their axis of symmetry and direction of propulsion.Though the particle' orientation fluctuates in time [Fig. 3B], their average orientation is primarily defined by the number of nearest neighbors as well as diffusiophoretic repulsion between clouds of chemicals from H_2O_2 decomposition by hematite[9,31]. Particles with 3-neighbors orient with $\bar{\phi}_3 \sim \pi/4$ and particles with 4-neighbors at $\bar{\phi}_4 \sim \pi/2$, where $\bar{\phi}_n$ is the average angle made by a swimmer with n neighbors with the local tangent [Fig.3A-B and SI]. The complex distribution of orientation fluctuations [Fig.3B], as well as additional experiments using rod-like structures of various length, for which the number of nearest neighbors is conserved but the velocity of the machine is changed [SI], highlight an additional and important role of hydrodynamics. It is, however, mostly neglected to devise a simple

model that predicts the dynamics of a machine from its geometry. The basic set of rules follows: particles with 1 or 2 neighbors are unstable and detach, particles with 3 or 4 neighbors exert forces on the perimeter and along their propulsion orientation, and particles with 5 or 6 neighbors do not contribute to the motion of the architecture [Fig.3A]. It underlies a simple model that only considers particles with 3 or 4 neighbors to predict the micromachines' dynamics from the template geometry. Each of those particles exert a point-force $F_{p,i} = \gamma V_S$, at the position M_i of particle i and along the direction $\mathbf{n_i}$ with angle $\bar{\Phi}_i$ defined primarily by the number of nearest neighbors. In addition, we assume that particles with 3-neighbors, for which the value of the angle is degenerate by symmetry, have the same angle that their nearest active 3-neighbors particle, emulating the hydrodynamic alignment observed in the experiment. We consider the machines to be solid bodies, as they do not deform when they displace. It follows that their dynamics are simply characterized by the translational velocity $\mathbf{v_G}$ of their geometric barycenter G and their instantaneous angular rotation Ω_G, which are obtained by balancing propulsive forces with the viscous drag. Recounting that vertical particles do not contribute to the 2D dynamics, we get:

$$\mathbf{v_G} = \frac{V_S}{N} \sum_{\varepsilon,i} \mathbf{n}_i \tag{1}$$

$$\mathbf{\Omega_G} = V_S \frac{\sum_{\varepsilon,i} \mathbf{GM_i} \wedge \mathbf{n_i}}{\sum_{all,j} \mathbf{GM_j}^2} \tag{2}$$

where $\sum_\varepsilon$ is the sum over the active edge, *i.e* swimmers with 3 or 4 neighbors and $\sum_{all}$, the sum over all N particles constituting the structure. Our simple model qualitatively captures the measured dynamics for 22 different colloidal architectures but overestimates rotation speeds by discounting fluctuations of orientation [Fig.3C-inset]. To account for their role, we record simultaneously the dynamics of a structure as well as the instantaneous positions and orientations of all constitutive particles. We observe quantitative agreement between the measured and predicted rotational [Fig. 3C] and translational speed [Fig.3D] for all time and for all structures, confirming the validity of the model and the role of geometry in programming the dynamics of a metamachine.

Remarkably, interactions between particles do not result from intrinsic properties but rather from the interplay between geometric arrangement and self-propulsion. As they reorient reversibly, otherwise identical particles reprogram autonomously to different functions in response to changes in the structure or their environment [Fig. 4A]. The ability for particles to reprogram autonomously allows reconfiguration and provides unmatched control to dynamical assembly. It highlights a salient advantage of the proposed strategy and contrasts with conventional assembly encoded in properties of the colloidal building blocks, e.g. shape[38] or specific interactions[11,13,15]. This feature is harnessed to assemble and reconfigure bespoke machines from a set of identical constitutive building blocks. For example, we devise a slender structure by template-and-merge of substructures, requiring particles to reprogram autonomously: particles previously sitting at the edge of templated metamachines become integrated to the interior of a slender structure [Fig.4B]. They spontaneously reorient to stand vertically, simultaneously annealing defects between merged substructures and providing cohesion to a novel architecture. It autonomously rotates. The architecture is reconfigured by application of a novel template: particles from the edge are ejected and a novel active boundary forms. Particles reprogram so that the particles now on the boundary reorient and contribute to the rotation of the structure [Fig.4B, movie S1].

We further design and assemble a broad range of colloidal metamachines. Chiral structures that rotate predictively [Fig.4C, D], or rotationally symmetric structures, which direction of rotation results from spontaneous symmetry breaking[9] following removal of the template [Fig.1C, movie S3]. In effect, only convex structures are accessible from direct templating: wrongful occupation of vacant positions in concave shapes due to attractive interactions otherwise prescribe the formation of the desired structures. We overcome this limitation using the spatiotemporal control offered by the SLM. We first assemble metamachines from convex templates and combine them with individual particles to obtain a stable dynamical architecture with concave edges [Fig.4C, E]. This template-and-merge allows the formation of more complex machines: rotators from centro-

symmetric objects, whose chirality results from the conversion of a particle on the edge with 3 neighbors (and exerting forces) into a particle with 5 neighbors solely contributing to the cohesion of the structure [Fig.4C, D]. The control offered by the SLM allows one to discriminate the particles undergoing activity annihilation and control the chirality of the final architecture from identical substructures. In order to demonstrate the broad applicability of the strategy, we devise by template-and-merge an autonomous translating metamachine, presenting a physical cavity to demonstrate the opportunities of metamachines to manipulate objects at the microscale [Fig.4E-F and Fig.1E, movie S4]. As effective interactions exert generically on all particles, we can program hybrid metamachines, using also optical patterns and passive particles as templates. The active heterodimers provide provide cohesion and force generation to the hybrid metamachine [Fig.1F and movie S5]. This further highlights the potential of pluripotent active colloids for self-assembly and provides a natural point of convergence between our design of metamachines and state-of-the-art colloidal design. This work offers a novel unique outlook for self-assembly. It harnesses forces exerted by active building to devise multi-fated particles, with reprogrammable (effective) interactions, that evolve reversibly and autonomously. It reinstates optical manipulation as a darling of assembly at the microscale by overcoming its equilibrium limitations. Our approach will further benefit from progress in colloidal design[11,12] to advance self-assembly. It also provides uncharted opportunities for the development of shape-shifting materials[39,40] and the development of machines made of machines.

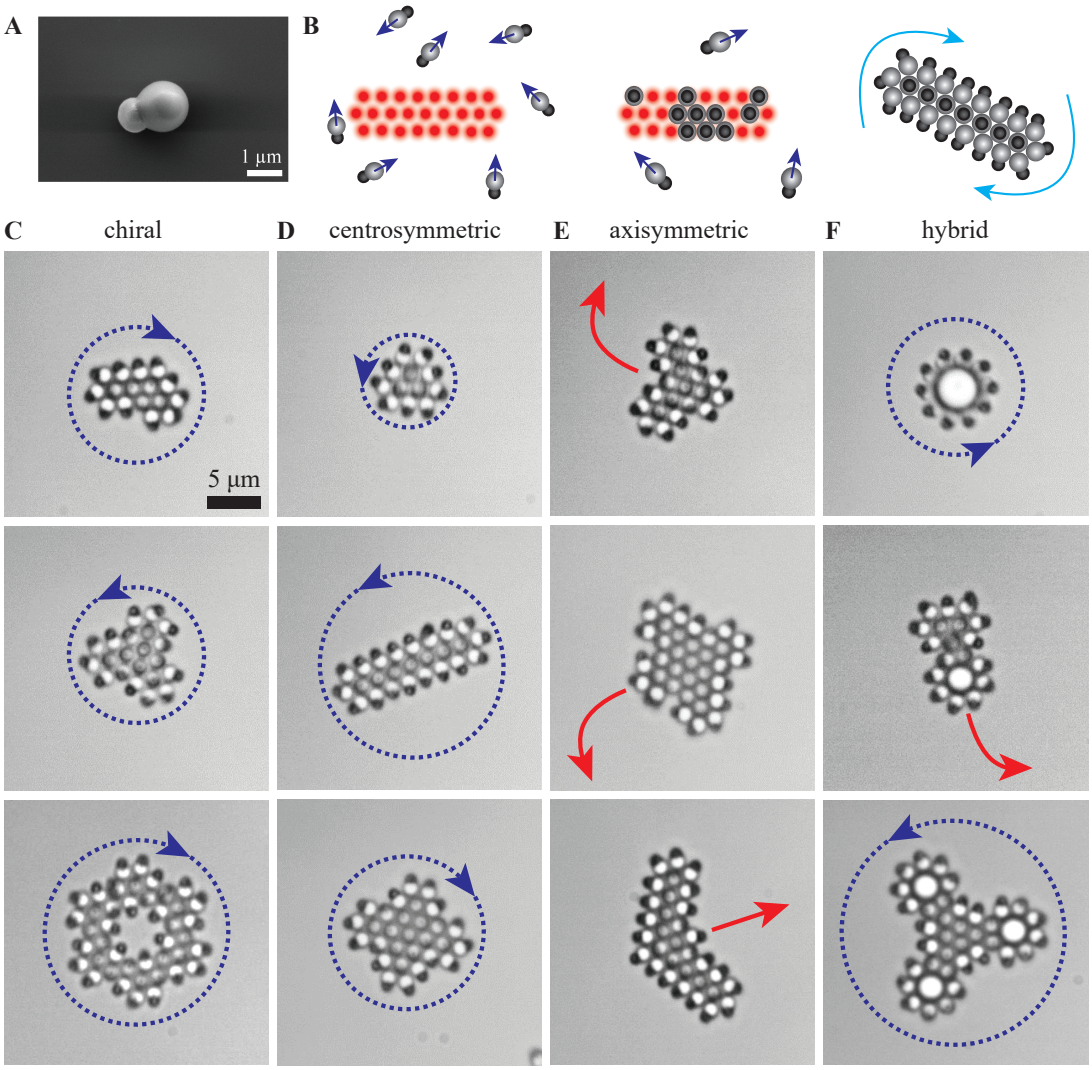

Figure 1: **Colloidal metamachines**. **A.** Scanning Electron Microscopy of a TPM-hematite heterodimer. **B.** Optical assembling of a metamachine. An optical pattern of traps is superimposed to the blue illumination activating the heterodimers. They travel randomly on the substrate until they encounter and optical trap and reorient vertically. In absence of propulsion, heterodimers are repelled by scattering by trapping laser. Upon removal of the optical template, the structure is stable, particles reorient and the structure exhibits autonomous dynamics [see Main Text]. **C-F.** Bright field pictures of colloidal metamachines. **C.** Chiral metamachines rotate in fixed direction, **D.** Centro-symmetric metamachines rotate by spontaneous symmetry breaking. **E.** Axisymmetric metamachines with translational motion. **F.** Hybrid metamachines composed of passive spheres and active heterodimers. Blue arrows indicate the direction of rotation, red arrows indicate the direction of propulsion. Identical scale for all images.

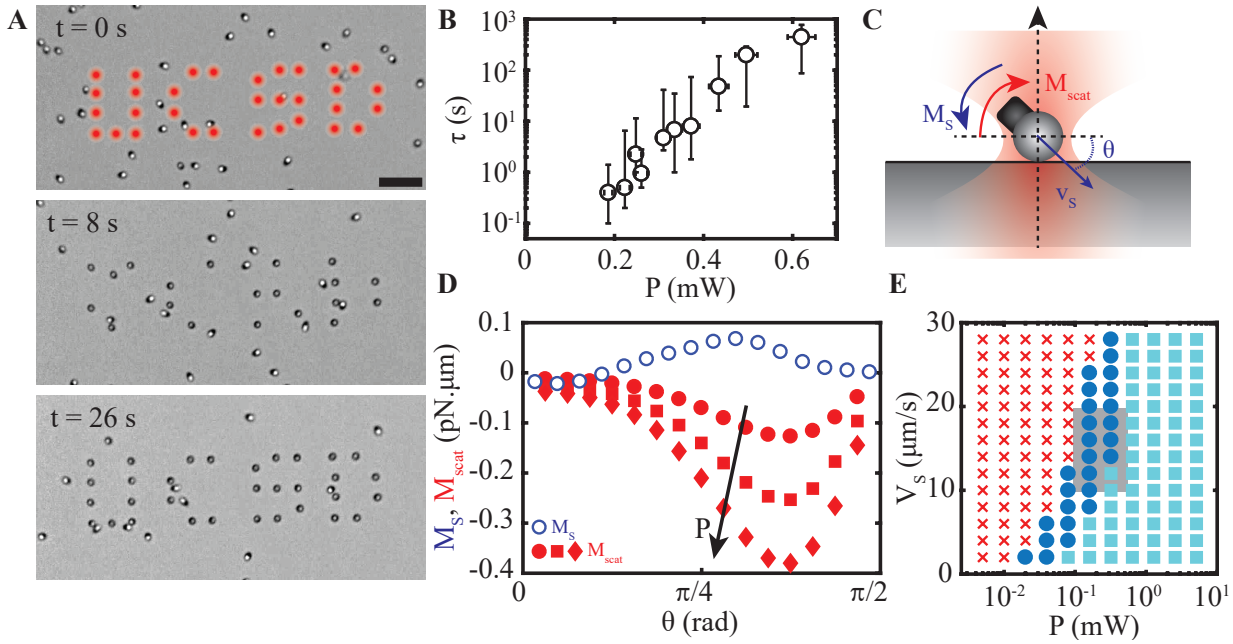

Figure 2: **Activity-assisted optical trapping**. **A.** Time lapse of active particles in a pattern of optical traps forming the letters UCSD. Enhanced diffusivity of self-propelled particles leads to rapid occupancy of the optical traps. Scale bar is 10 μm. **B.** Trapping lifetime τ of a microswimmer measured at different incident laser power P. Stable trapping is achieved for $P \gtrsim 0.5$ mW. **C.** Trapping process. Gradient forces pull the particle at the center, while scattering forces on the hematite exert a torque $M_{scat}(\theta)$ on the heterodimer. It is balanced by $M_S(\theta)$ resulting from the interaction of the swimmer with the substrate. Self-propulsion at speed V_S opposes scattering forces and leads to stable trapping near focus. **D.** Experimental measurement of the torque M_S (empty blue circles), and numerical determination of M_{scat} (full red symbols) for a swimmer with the TPM bead at the center of the focus for increasing incident power P: 0.25 (circles), 0.5 (squares), and 0.75 (diamonds) mW. **E.** Simulated phase diagram $\{P, V_S\}$ for active heterodimers entering a trap with incident power P with velocity V_S, in the absence of noise. The outcome results from the interplay between activity and optical forces. When reaching an optical trap, a swimmer can cross it (red crosses), be ejected by radiation pressure (cyan squares), or be trapped (blue circles). The grey rectangle overlays the range of values in the experiment, showing quantitative agreement with the numerical model.

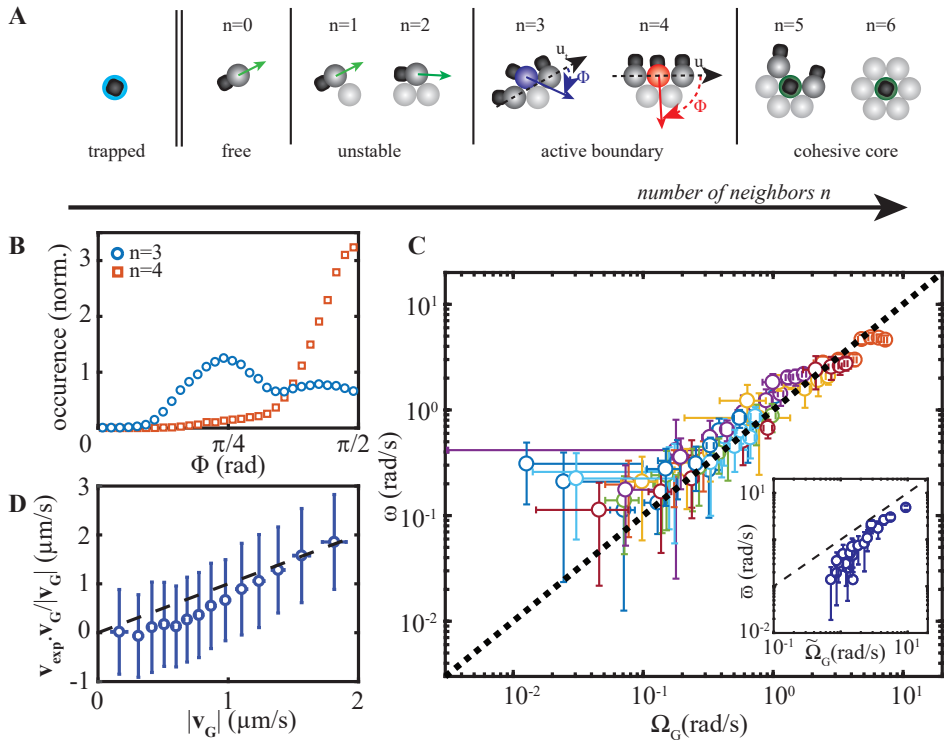

Figure 3: **Pluripotent colloids. A.** Heterodimers exhibit different functions as a function of their number of neighbors n. Heterodimers stand vertically in an optical trap (light blue). For $n = 0$ heterodimers navigate freely. For $n = 1$ or 2, the structure is unstable and the heterodimers detach. For $n = 3$ (purple) or 4 (red), heterodimers orient with respect to the local tangent $\mathbf{u_t}$, with $\bar{\Phi}_3 \sim \pi/4$ and $\bar{\Phi}_4 \sim \pi/2$, respectively and exert a force along their propulsion direction. For $n = 5$ or 6 (green), heterodimers are vertical and exert attractive interactions. **B.** Histograms of the angles Φ of heterodimers for $n = 3$ (blue circles) and $n = 4$ (red squares) obtained from analysis of slender micromachines of different lengths. **C.** Measured angular velocities ω for 22 different machines (1 color and 4 data points per machine), plotted against the prediction Ω obtained by tracking of the instantaneous orientation and position of all constitutive swimmers in eq.(2). **C-inset.** Mean value $\bar{\omega}$ plotted against $\bar{\Omega}$ predicted from our simple model with fixed orientations $\Phi(n = 3) = \pi/4$ and $\Phi(n = 4) = \pi/2$ [see Main Text]. **D.** Projected translational speed measured by averaging data from all 22 structures plotted against the predicted translational speed $\mathbf{v}_\mathrm{G}$ from eq.(2). Black dashed lines in C and D indicate unity slopes.

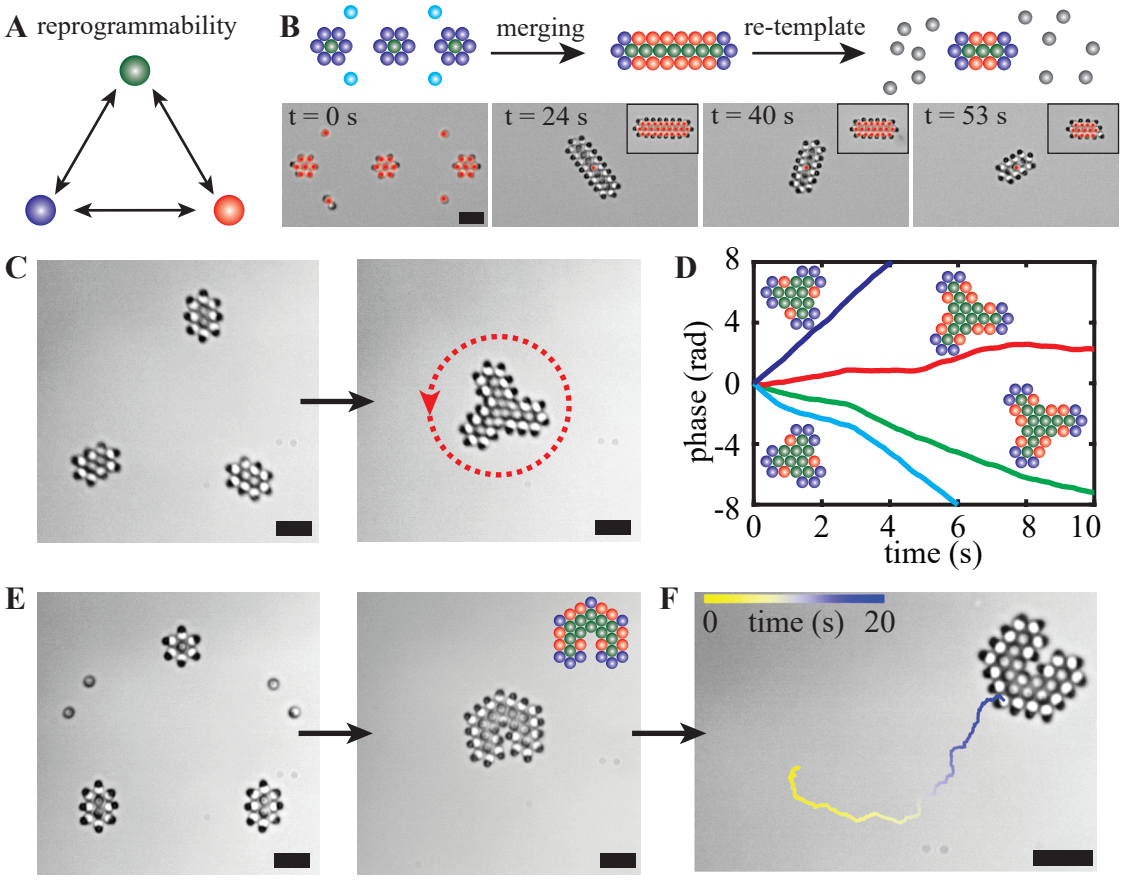

Figure 4: **Reprogrammable Metamachines**. **A.** Heterodimers reprogram autonomously and change functionality (colors as in Fig. 3A). **B.** Metamachine Reconfiguration. *(top)* : Schematic of the reconfiguration process. Colors indicate the functions as defined in Fig.3A. They highlight the autonomous reprogrammation of the particles as the structure reconfigures. Substructures are templated then merged to build a slender metamachine. Changes in templates lead to reconfiguration of the machine enabled by the autonomous reprogrammation of the constitutive particles. *bottom*: Experiment time-lapse. Red circles indicate optical traps, used for re-templating and practical pinning of the structure. Insets : optical patterns for re-templating. **C.** Formation of chiral structures by template-and-merge. The dashed arrow indicates the direction of rotation. **D.** Rotational dynamics of 4 different chiral structures with diagrams highlighting the role of red ($n = 4$) swimmers to set the chirality. **E.** Assembly of a translational metamachine by template and merge. The diagram highlights the role of green ($n = 5$) swimmers at the concave angle to introduce the forward/backward asymmetry and persistent self-propulsion of the machine, presented in **F.**. Scale bars are 5 μm.

Materials and Methods

Synthesis of hematite cubes The synthesis procedure of hematite cubes follows the sol-gel method described by Sugimoto[41]. Briefly, we mix 100 mL of 2M $FeCl_3 \cdot 6H_2O$, 90 ml 6 NaOH and 10 ml water, in a 250 mL pyrex bottle and shake thoroughly. Immediately after, the bottle is placed in an oven at $100°$C, and aged for 3 to 4 days, until the hematite particles reach the desired size (growth is monitored by optical microscopy). The resulting hematite cubes in the gel network are isolated by successive sedimentation and resuspension cycles in DI water [Fig.S1].

Synthesis of heterodimers The synthesis of heterodimer particles is performed by heterogeneous nucleation of trialkoxysilanes (oil precursors) on solid hematite particles as seeds, and the control of their wetting properties with the pH of the solution. The synthesis procedure is adapted from ref.[28], with chemical modification to reinforce the stability of the heterodimer under light illumination. In particular, we make use of a hydrophobic copolymer Hexadecyltrimethoxysilane (HTS) to chemically protect the bond between the hematite and polymer core against highly reactive hydroxil radicals generated during H_2O_2 consumption. A beaker with 100 mL of DI water is prepared, and mixed with 120 μL of a 50% NH_3 solution, giving a pH ~ 10.5. The solution is kept under mild magnetic stirring. We add $\sim$ 1 mL of an aqueous solution of hematite particles, to get a slightly red-colored solution. Following, we add 100 μL of HTS, immediatly followed by 500 μL of 3-(Trimethoxysilyl)propyl methacrylate (TPM). The solution is then covered with parafilm, and let under mild stirring for $\sim$ 2h00. During this time, the HTS and TPM hydrolyse, and condense on the hematite particles, with strong wetting leading to their engulfment in the oil phase. After $\sim$ 2h00, the solution is turbid, as a result of the scattering of newly formed colloidal particles. We then add 2 mL of Pluronic F-108 solution (5% wt), and wait 2 mn. The dewetting and extrusion of TPM from the hematite is performed by changing the pH of the solution to pH $\sim$ 2.1, by adding 1.5 mL of 1M chloridric acid HCl. The solution is let under stirring for 3 mn,

and diluted 4 times. We then carry out the polymerization by adding 50 mg of radical initiator Azobisisobutyronitrile (AIBN) to the solution and leave it under stirring for ~ 5 mn. The beaker is covered with an aluminium foil and placed in a pre-heated oven at $\sim$ 80 degrees Celsius for 2 hours. We let the solution cool down to room temperature, remove the excess solution above the sedimented particles, and add 50 mL DI water with 1 mL of 250 mM NaOH solution, giving a pH ~ 10, and let the solution overnight to facilitate the hydrolysis and condensation of any remaining HTS monomers. The solution is then centrifuged and rinsed multiple times to remove the excess TPM/HTS particles and obtain the desired colloidal solution of heterodimers.

Sample preparation The samples are prepared at low particle density of $\sim 10^{-3}$ μm^{-2}. The heterodimer particles are diluted in a 6% solution of hydrogen peroxide H_2O_2 (Fisher Scientific H325-500) in deionized water (Milli-Q, resistivity 18.2M). The cell for the solution is composed of a rectangular capillary glass (VitroCom 3520-050), previously subjected to plasma cleaning (Harrick Plasma PDC-001) and thoroughly rinsed with DI water. The solution is injected in the capillary, then sealed with capillary wax (Hampton Research HR4-328). As the particles are non-buoyant, they sediment near the bottom surface of the capillary, and observation with the microscope is made in this plane.

Optical setup The experiments are carried out on a custom-made optical setup, allowing for simultaneous uniform excitation of the microswimmers and holographic optical tweezing, as presented on [Fig.S2]. The sample is observed with bright-field transmitted illumination (LED1). A LED is set up in the blue range (LED2, $\lambda = 425 - 500$ nm, Lumencor SOLA 6-LCR-SC) and uniformly illuminates the sample on a large area (size $\sim 300 \times 300$ μm^2) to activate the swimmers by triggering the photocatalytic decomposition of H_2O_2 by the hematite (typical intensity of $\sim 1\,\mu$W/μm^2). A red continuous laser with near TEM00 mode ($\lambda = 639$ nm, Coherent, Genesis

MX639-1000 STM, $M^2 < 1.1$) is added on the optical path. The linearly polarized beam is collimated, rotated with a $\lambda/2$ waveplate, and sent on the surface of a Spatial Light Modulator (SLM, Holoeye -LETO Phase Only Spatial Light Modulator). The optical path follows a typical 4-f setup using two $f_1 = 400$ mm lenses, and the zero-order of the diffracted beam is filtered out with a diaphragm at equal distance $d = f$ between the two lenses. Following, a hologram is formed at the back aperture of a high NA objective (Nikon apo-TIRF, $\times 100$, NA=1.45) allowing for the creation of complex spatiotemporal optical patterns in the object plane, at the bottom surface of the sample. The hologram is computed in real time using a computer software (Holoeye), with the phase patterns computed under Matlab, and allows for the selective trapping and manipulation of individual swimmers. An electronic shutter (Thorlabs SHB1T) on the red optical path enables switching ON and OFF the laser traps. The sample is mounted on a manual micrometric stage (Nikon Ti-SR). Observation is performed through the same objective as for excitation, and the bright-field signal is reflected on a polarizing beam splitter and observed on 2 monochrome Charged Coupled Devices (CCDs) with different resolutions (0.05 μm/px and 0.1 μm/px, respectively, Edmund Optics EO-1312M), with appropriate spectral filters.

Image acquisition and analysis : All experiments were recorded on the CCD camera with 0.05 μm/px resolution (except for movie S2 performed at lower magnification), at frame rate between 20-50 fps, and under bright field illumination. Tracking was performed separately for the hematite and TPM particles with standard Matlab routine. For each of the 22 investigated structures, we record at least 10 s of experiments. The positions are then averaged a first time over 200 ms to compute $\omega(t)$, $\Omega(t)$, $\mathbf{v}_G(t)$; and further averaged to obtain 4 data points with equivalent statistical weight [Fig. 3C]. Error bars are obtained from standard deviations of experimental measurements.

Analytical calculation of the optical field The system is in the Mie regime, and uses a strongly focused laser beam (NA $\sim$ 1). We therefore use exact formulas for the optical forces acting on an a homogeneous sphere of any composition in the Mie-regime, formalized upon the Generalized Lorenz-Mie Theory (GLMT) for a highly focused incident gaussian beam in the angular spectrum representation. Knowing the full expressions of the scattered fields, the optical forces are obtained by integrating the Maxwell Stress tensor over a surface surrounding the particle. The full expressions of F_x, F_y, and F_z and their complete derivation is described in Ref.[33]. We consider an incident beam at $\lambda = 639$ nm filling the entire back aperture of a water (refractive index $n_w = 1.33$) immersion objective, polarized along X and propagating along the Z-direction. We chose the parameters of the optics as to get a waist of $\omega_0 \approx 400nm$ that closely matches the experimentally determined value [Fig.S4]. The TPM part of the heterodimer is modeled as a non-absorbing dielectric bead of refractive index $n_T = 1.51$ and radius $R_T = 500$ nm, and the hematite part is modeled as a spherical body of radius $R_H = 250$ nm, homogeneously filled with $\alpha-\mathrm{Fe_2O_3}$ ($n_H = 3.10 + 0.065i$ at $\lambda = 639$ nm). The analytical expression, from Ref.[33], calculates the forces on individual TPM and hematite particles, that we use to approximate the total force on a heterodimer [Fig.S6].

Numerical calculation of the optical field We use Comsol Multiphysics (v5.5) to compute the 3D optical field generated by a single, focused laser beam in presence of a *full* heterodimer particle in water. The solution for the background field is analytically approximated using the angular spectrum representation of the focal field for a non-paraxial beam, and using discrete summation to approximate the continuous integration over the numerical aperture of the focusing lens.

We model infinite boundaries in our system using the Perfectly Matched Layers module of COMSOL, which prevents any reflection of the scattered field on our artificial boundaries. The optical forces F_x, F_y, F_z are then obtained by integrating the Maxwell stress tensor on the surface of the particles[32]. We check the incident power by integrating the flux of the Poynting vector

associated to the background field across the transverse XY plane.

The results are compared to the total force obtained by summation of the forces exerted on individual TPM and hematite particles, computed using analytical expressions [Fig.S6]. We observe a relative difference between the two estimation below 20%, showing that the total force is well approximated by individually calculating the optical forces on a single hematite and a single TPM particle, and summing them after. We note that for single particles, the forces computed with COMSOL agree perfectly with the theory above for identical beam parameters. We therefore use this method for mapping of the optical forces in the $\{X, Z, \theta\}$ space.

Motion of a self-propelled heterodimer entering an optical trap - simulations We consider a simplistic model where the heterodimers are self-propelled particles in the absence of noise. Heterodimers are considered rigid bodies constituted of 2 distinct parts in the XZ plan, with orientation $\mathbf{u}_\theta$. The position $\mathbf{r} = \{x, y = 0, z\}$ is defined as $\mathbf{r} = [\gamma_H \mathbf{r_H} + \gamma_T \mathbf{r_T}]/(\gamma_H + \gamma_T)$ to account for the different drag coefficients $\gamma_H = 6\pi\eta R_H$ and $\gamma_T = 6\pi\eta R_T$ acting on the hematite and TPM beads situated at $\mathbf{r_H}$ ad $\mathbf{r_T}$, respectively. In our model, we discard hydrodynamic interactions between the hematite and the TPM. The equations of motion are determined from balancing external forces and self-propulsion by the viscous drag, i.e. : $\sum \mathbf{F}_{ext} = \mathbf{F}_{drag}$ and $\sum \mathbf{M}_{ext} = \mathbf{M}_{drag}$.

The total drag torque is obtained as $M_{drag} = \Gamma\omega$, with $\Gamma = \gamma_H {R_T}^2 + \gamma_T {R_H}^2 + (4/3)(\gamma_H R_H^2 + \gamma_c R_T^2)$. For a swimmer with propulsion velocity V_S, we write :

$$\frac{dx}{dt} = V_S \cos(\theta) + \frac{\sum F_{ext,x}}{\gamma} \tag{3}$$

$$\frac{dz}{dt} = V_S \sin(\theta) + \frac{\sum F_{ext,y}}{\gamma} \tag{4}$$

$$\frac{d\theta}{dt} = \frac{1}{\Gamma} \sum M_{ext} \tag{5}$$

We simulate the motion of particles in the presence of optical forces, acting independently

on the particles, using finite-difference equations as derived from eq.3-5. We consider the linear optical regime, such that the optical forces $F_{opt} \propto P_{inc}$, with P_{inc} the incident power. We model the substrate as an impenetrable wall situated at $z = -R_T$, such that any step for which the particle penetrates the wall yields to a displacement of the swimmer to be in close contact with the wall, i.e. we force $z_T \geq 0$, and $z_H \geq R_H - R_T$. We obtain $M_S(\theta)$ by interpolation from the experimental values, and apply the same procedure for the optical potential $M_{scat}(\mathbf{r}, \theta)$: we extract the forces applied on the hematite and TPM parts individually, allowing us to approximate both torques and forces $F_{scat,x,z}(\mathbf{r}, \theta)$ acting on the heterodimer.

The torque $M_S(V_S, \theta)$ depends on the instantaneous propulsive force (i.e velocity V_S) of the swimmer. In the Stokes regime ($Re << 1$), we can reasonably assume both phoretic and hydrodynamic effects to be linearly dependent on the velocity of the swimmer. Hence, we assume linear dependency of $M_S(V_S, \theta)$, such that $M_S(V_S, \theta) = (V_S/V_{S,0})M_S(\theta)$, where $V_{S,0} = 16$ μm/s is the velocity of the swimmer in free space. Finally, the gravitational torque is negligible to the typical values for M_{scat} and M_S, and the effect of the gravitational torque is therefore not included when computing the trajectories.

References and Notes

1. Dreyfus, R. et al. Microscopic artificial swimmers. Nature **437**, 862–865 (2005).

2. Alapan, Y., Yigit, B., Beker, O., Demirörs, A. F. & Sitti, M. Shape-encoded dynamic assembly of mobile micromachines. Nature Materials **18**, 1244–1251 (2019).

3. Needleman, D. & Dogic, Z. Active matter at the interface between materials science and cell biology. Nature Reviews Materials **2**, 17048–14 (2017).

4. Keber, F. C. et al. Topology and dynamics of active nematic vesicles. Science **345**, 1135–1139 (2014).

5. Zhang, S. et al. The optoelectronic microrobot: A versatile toolbox for micromanipulation. Proceedings of the National Academy of Sciences of the U.S.A **116**, 14823–14828 (2019).

6. Maggi, C. et al. Self-Assembly of Micromachining Systems Powered by Janus Micromotors. Small **12**, 446–451 (2015).

7. Di Leonardo, R. et al. Bacterial ratchet motors.
Proceedings of the National Academy of Sciences of the U.S.A **107**, 9541–9545 (2010).

8. Sokolov, A., Apodaca, M. M., Grzybowski, B. A. & Aranson, I. S. Swimming bacteria power microscopic gears.
Proceedings Of The National Academy Of Sciences Of The United States Of America **107**, 969–974 (2010).

9. Aubret, A., Youssef, M., Sacanna, S. & Palacci, J. Targeted assembly and synchronization of self-spinning microgears. Nature Physics **14**, 1–5 (2018).

10. Miskin, M. Z, Alejandro J, Dorsey, K. Esposito, E. P Reynolds, M. F, Michael F, Liu, Q., Cao, M., Muller, D. A, McEuen, P. L & Cohen, I. Electronically integrated, mass-manufactured, microscopic robots. Nature **584**, (2020).

11. He, M. et al. Colloidal diamond. Nature **585** (2020).

12. Gong, Z., Hueckel, T., Yi, G.-R. & Sacanna, S. Patchy particles made by colloidal fusion. Nature **550**, 234–238 (2017).

13. Wang, Y. et al. Colloids with valence and specific directional bonding. Nature **490**, 51–55 (2012).

14. Damasceno, P. F., Engel, M. & Glotzer, S. C. Predictive Self-Assembly of Polyhedra into Complex Structures. Science **337**, 453–457 (2012).

15. Chen, Q., Bae, S. C. & Granick, S. Directed self-assembly of a colloidal kagome lattice. Nature **469**, 381–384 (2011).

16. Grier, D. G. A revolution in optical manipulation. Nature **424**, 810 (2003).

17. Palagi, S. & Fischer, P. Bioinspired microrobots. Nature Reviews Materials **3**, 1–12 (2018).

18. Li, S. et al. Particle robotics based on statistical mechanics of loosely coupled components. Nature **567**, 1–6 (2019).

19. Rubenstein, M., Cornejo, A. & Nagpal, R. Robotics. Programmable self-assembly in a thousand-robot swarm. Science **345**, 795–799 (2014).

20. Howse, J. R. et al. Self-Motile Colloidal Particles: From Directed Propulsion to Random Walk. Physical Review Letters **99**, 048102 (2007).

21. Bricard, A., Caussin, J.-B., Desreumaux, N., Dauchot, O. & Bartolo, D. Emergence of macroscopic directed motion in populations of motile colloids. Nature **503**, 95–98 (2014).

22. Bazant, M. Z. & Squires, T. M. Induced-charge electrokinetic phenomena: Theory and microfluidic applications. Physical Review Letters **92**, 066101 (2004).

23. Ren, L. et al. 3D steerable, acoustically powered microswimmers for single-particle manipulation. Science Advances **5**, eaax3084 (2019).

24. Melde, K., Mark, A. G., Qiu, T. & Fischer, P. Holograms for acoustics. Nature **537**, 518–522 (2016).

25. Frangipane, G. et al. Dynamic density shaping of photokinetic E. coli. eLife **7** (2018).

26. Arlt, J., Martinez, V. A., Dawson, A., Pilizota, T. & Poon, W. C. K. Painting with light-powered bacteria. Nature Communications **9**, 1–7 (2018).

27. Palacci, J., Sacanna, S., Steinberg, A. P., Pine, D. J. & Chaikin, P. M. Living Crystals of Light-Activated Colloidal Surfers. Science **339**, 936–940 (2013).

28. Youssef, M., Hueckel, T., Yi, G.-R. & Sacanna, S. Shape-shifting colloids via stimulated dewetting. Nature Communications **7**, 12216 (2016).

29. Curtis, J. E., Koss, B. A. & Grier, D. G. Dynamic holographic optical tweezers. Optics Communications **207**, 169 – 175 (2002).

30. Anderson, J. Colloid transport by interfacial forces. Annual Review of Fluid Mechanics **21**, 61–99 (1989).

31. Aubret, A. & Palacci, J. Diffusiophoretic design of self-spinning microgears from colloidal microswimmers. Soft Matter **14**, 9577–9588 (2018).

32. Sukhov, S. & Dogariu, A. Non-conservative optical forces. Reports on Progress in Physics **80**, 112001 (2017).

33. Neves, A. A. R. & Cesar, C. L. Analytical calculation of optical forces on spherical particles in optical tweezers: tutorial. J. Opt. Soc. Am. B **36**, 1525–1537 (2019).

34. Uspal, W. E., Popescu, M. N., Dietrich, S. & Tasinkevych, M. Self-propulsion of a catalytically active particle near a planar wall: from reflection to sliding and hovering. Soft Matter **11**, 434–438 (2015).

35. Spagnolie, S. E. & Lauga, E. Hydrodynamics of self-propulsion near a boundary: predictions and accuracy of far-field approximations. Journal of Fluid Mechanics **700**, (2012).

36. Weinert, F. M. & Braun, D. Observation of Slip Flow in Thermophoresis. Physical Review Letters **101**, 168301 (2008).

37. Di Leonardo, R., Ianni, F. & Ruocco, G. Colloidal Attraction Induced by a Temperature Gradient. Langmuir **25**, 4247–4250 (2009).

38. Sacanna, S. & Pine, D. J. Shape-anisotropic colloids: Building blocks for complex assemblies. Current Opinion in Colloid & Interface Science **16**, 96–105 (2011).

39. Nguyen, T. D., Jankowski, E. & Glotzer, S. C. Self-Assembly and Reconfigurability of Shape-Shifting Particles. Acs Nano **5**, 8892–8903 (2011).

40. Banerjee, D., Souslov, A., Abanov, A. G. & Vitelli, V. Odd viscosity in chiral active fluids. Nature Communications **8**, 1–12 (2017).

41. Sugimoto, T., Itoh, H. & Mochida, T. Shape control of monodisperse hematite particles by organic additives in the gel-sol system. Journal of Colloid and Interface Science **205**, 42 – 52 (1998).

Acknowledgments The authors thank R. Jazzar for useful advice regarding the synthesis of heterodimers. We thank S. Sacanna for critical reading. This material is based upon work supported by the National Sci-

ence Foundation under Grant No. DMR-1554724 and Department of Army Research under grant W911NF-20-1-0112.

Competing Interests The authors declare that they have no competing financial interests.

Correspondence Correspondence and requests for materials should be addressed to A. Aubret (antoine.aubret@u-bordeaux.fr) and J. Palacci (palacci@ucsd.edu).

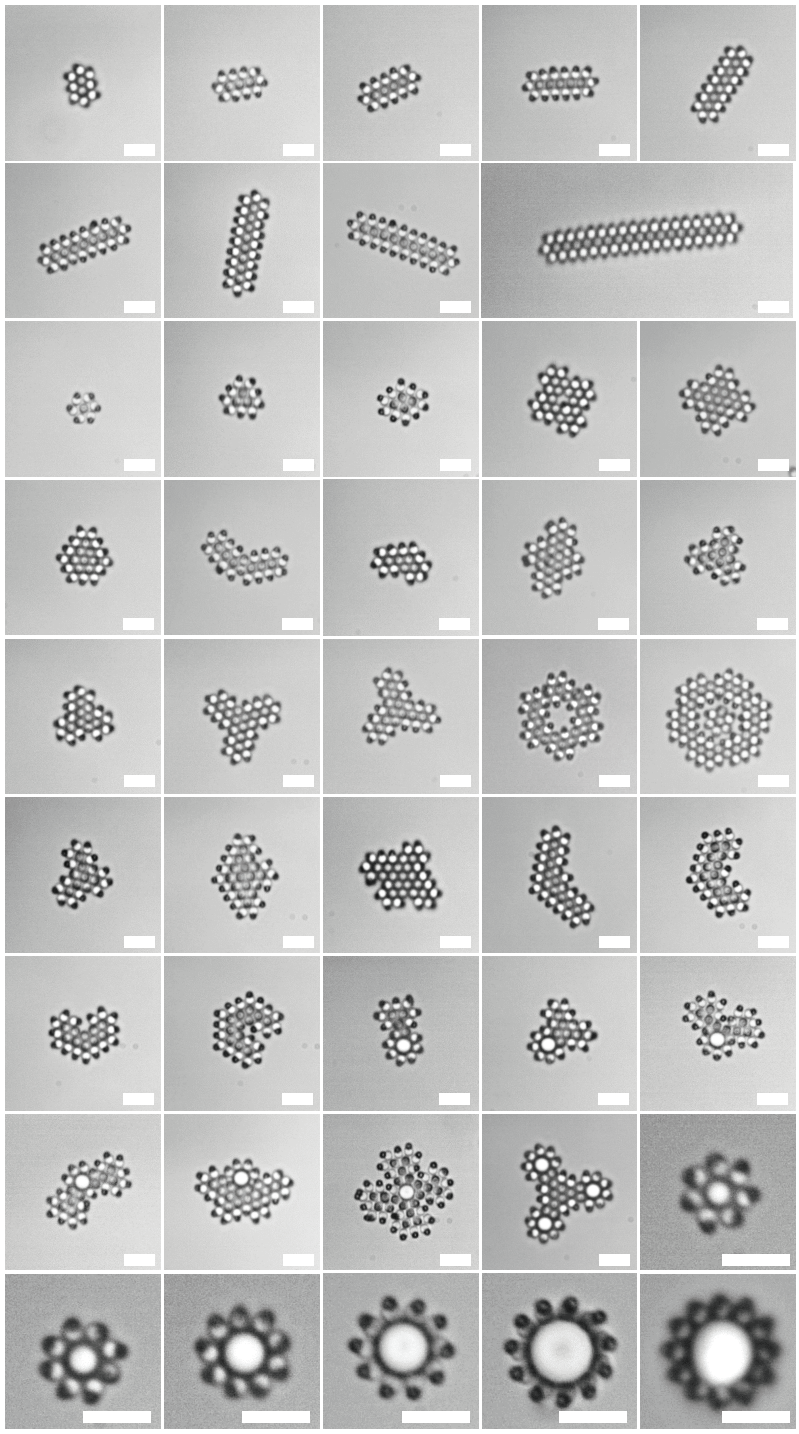

Extended Figure 1. List of Colloidal Metamachines. Bright field images of the 44 metamachines assembled and studied for the present work. All scale bars are $5\mu m$.

Supplementary Information for : Metamachines of Pluripotent Colloids

Antoine Aubret,[1,2*] Quentin Martinet,[1] Jeremie Palacci[1*]

[1]Department of Physics, University of California San Diego
[2]Current Address: Univ. Bordeaux, CNRS, LOMA, UMR 5798, F-33405 Talence, France

1 Description of Movie Materials

All movies are recorded in bright-field illumination.

Supplementary Video 1: Re-programmable metamachines. Self-propelling heterodimers are assembled into metamachines using patterns of optical traps. The traps uniquely serve to assemble the desired machine and are removed after iniatition, letting the machine to evolve autonomously. Spinning structures are first formed and merged to form a larger metamachine: a slender structure that autonomously rotates. The metamachine reconfigures following optical re-templating. Heterodimers in the metamachine reprogram autonomously and reorient, reversibly changing function. Turning off the blue light and removing the heterodimer activity, the system returns to equilibrium, the dynamics and interactions vanish. Heterodimers diffuse thermally and the metamachine breaks down. The successive templates are indicated in red at the bottom-right of the frames. The acceleration of the movie with respect to real time is indicated on the movie: sped-up 10 times for the formation of the substructures, and 2 times for the re-templating process.

Supplementary Video 2 : Activity-assisted optical trapping. A *static* pattern of 31 optical traps forming the letters "UCSD" is set on a field of view $\sim 10^4 \mu m^2$. Active heterodimers self-propel with a persistent random walk leading to a diffusive behavior with effective diffusivity $D \sim 110 \mu m^2/s$, 2 or 3 orders of magnitude above thermal diffusion. As they cross an optical trap, the heterodimers reorient, stand vertically, propelling against the substrate. The rapid diffusion of the self-propelled articles leads to rapid occupation (~ 30 s) of the individual traps forming the letter "UCSD", avoiding the tedious pick-and-place required for optical trapping of microscopic objects. The movie is sped-up 2 times compared to real time.

Supplementary Video 3: Chiral metamachines. Centrosymmetric metamachines (assembly not shown but obtained using optical templates as shown previously) are merged to form a chiral metamachine. The chirality of the metamachine results from the conversion of particles laying flat on the edge into vertical particles as centrosymmetric metamachines merge. By controlling where the centrosymmetric metamachines meet and merge, we obtain two metamachines of opposite chirality and opposite rotation directions. Real-time movie.

Supplementary Video 4: Translational metamachine. Assembly of a translational metamachine by template and merge of centrosymmetric metamachines (assembly not shown but obtained using optical templates as shown previously) and heterodimers trapped individually. It highlight the role of the heterodimers in the concave region of the metamachine to introduce the forward/backward asymmetry and persistent self-propulsion of the machine. Real-time movie.

Supplementary Video 5: Hybrid metamachines. The design of metamachines is extended by inclusion of passive particles to the machine. Here, passive beads are trapped and surrounded by individual optical traps to form hybrid metamachines made of active heterodimers. They are further merged to form a large hybrid metamachine. Real time movie.

2 Supplementary Data and Experiments

2.1 Dynamics of the swimmers under homogeneous illumination

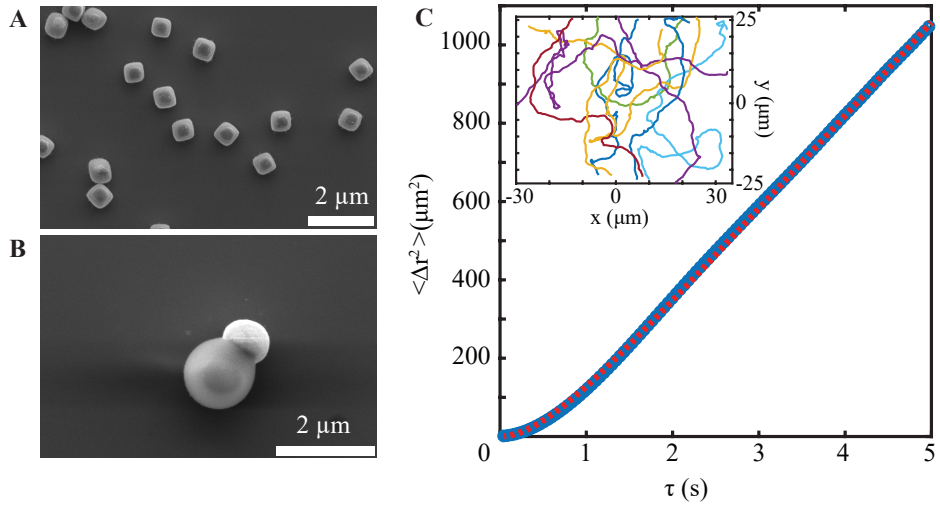

Fig. S1: **Characterization of the particles :** Scanning Electron Microscopy (SEM) images for **A** hematite cubes and **B** the heterodimer particles used in this work. **C**. Averaged Mean Square Displacement (MSD, blue circles) for the swimmers under blue light illumination only. The red dashed curve is a fit using eq.(1), fixing $D_T = 0.3$ μm^2/s, and giving $\tau_r = 1.1$ s and $v_S = 14.6$ μm/s as fitted parameters. *Inset :* typical trajectories of the swimmers, showing persistent random walk dynamics.

Under constant blue illumination, the heterodimers exhibit persistent random walk, and both their velocity v_S and persistence time τ_r are extracted from analysis of their 2D mean square displacement $< \Delta r(\Delta t)^2 >$, which follows (*1, 2*) :

$$< \Delta r(\Delta t)^2 >= 4D_T\Delta t + \frac{v_S^2\tau_r^2}{2}[\frac{2\Delta t}{\tau_r} + e^{-2\Delta t/\tau_r} - 1] \quad (1)$$

From fitting of the curve in [Fig.S1], we find $\tau_r = 1.1$ s and $v_S = 14.6$ μm/s.

2.2 Experimental setup

The experimental setup is described in [Fig.S2]. See [Material and Methods] for full description.

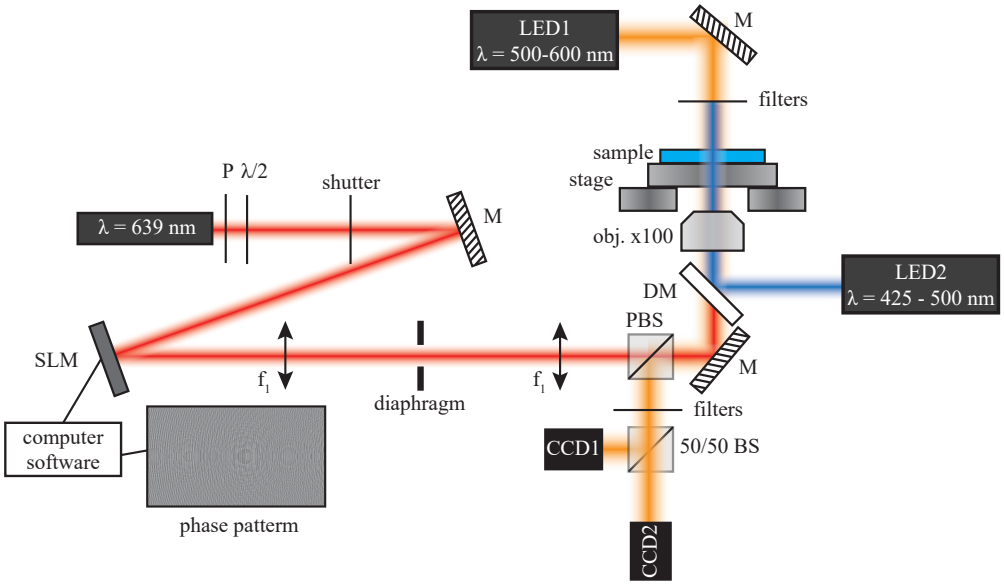

Fig. S2: **Optical setup.** For better clarity, not all optical elements are represented. The letters stand for : P - Polarizer, $\lambda/2$ - half-waveplate, M - Mirror, SLM - Spatial Light Modulator, PBS - Polarizing Beam Splitter, BS - Beam Splitter, DM - Dichroic Mirror.

2.3 Empirical determination of $\mathrm{M_S}$

We empirically extract and quantify the interaction of our swimmers with the surface from a statistical analysis of the angular position of the heterodimers [Fig.S3]. We record $\approx$ 12000 seconds of individual swimmers trajectories at a rate of 40 fps. For each trajectory, we independently track the positions of the hematite and TPM particles. The distribution of distances d between the two parts gives an approximate angular position as $\cos(\theta(t)) \sim d(t)/\max(d)$, assuming an orientation of the swimmer $\theta \in [0, -\pi/2]$. This gives the angular probability density function $P(\theta)$ at constant height, assuming that the swimmer does not significantly

leave the wall over the course of the trajectory, i.e. $z/R_T \ll 1$, R_T being the radius of the TPM bead. From this, we extract the effective interaction potential with the surface as $V(\theta) = -k_b T \ln P(\theta)$, and $M_S(\theta) = -d_\theta V(\theta)$. The results show that the swimmer mostly slides with a tilt angle of $\theta_0 \sim -\pi/8$ above the surface, as a result of its effective interaction with the surface. The extracted torque holds for a swimmer velocity of $V_{S,0} = v_S/\cos\theta_0 \approx 16$ μm/s.

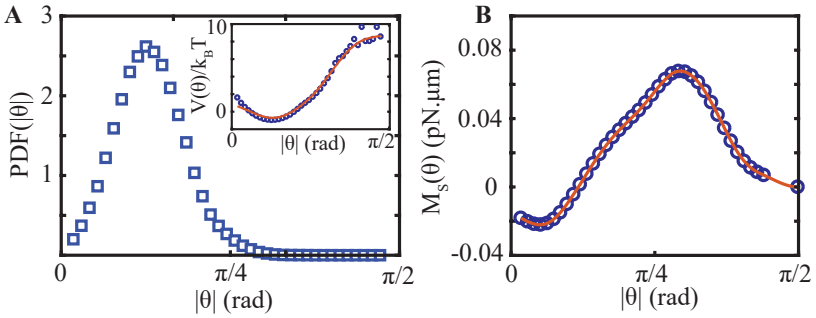

Fig. S3: **Experimental determination of the torque acting on a swimmer near a surface. A**. Probability Density Function PDF($|\theta|$) of the measured angle of the microswimmers. It shows a clear peak at $|\theta| = \pi/8$, while the probability of having a free vertical swimmer ($|\theta| = \pi/2$) is close to zero. *Inset :* Extracted effective potential $V(\theta)/k_B T$. **B** Plot of the torque $M_S(\theta)$, showing a maximum torque of ~ 0.08 pN·μm at $|\theta| \sim \pi/3$.

2.4 Hybrid architectures

Hybrid architectures composed of passive and active beads are built using the same optical templating method as described in the main text. Passive beads are trapped at their center, and surrounded by an integer number of individual traps for microswimmers [Extended Data Figure 1]. For beads surrounded by 7, 8, 9, 10, or 11 swimmers, we used pluronic F108 coated TPM beads, synthesized as described in Ref. (*3*). For beads surrounded by 12 or 13 swimmers, we used commercially available 7 and 8 μm polystyrene beads (Sigma Aldrich).

2.5 Characterization of the laser profile

Experimental determination

We measure the width of the laser spot from the reflection of the laser beam on the glass/water interface, imaged on the CCD camera, at resolution of 0.03 μm/px [Fig.S4A]. Substracting background noise, the intensity profile is well fitted by a gaussian curve, from which we extract $\sigma = 210 \pm 10$ nm, which corresponds to a waist $\omega_0 \sim 2\sigma = 420$ nm.

2.6 Simulations

We use the angular spectrum representation of a strongly focused laser beam to compute the optical forces acting on the particles (*4*) (hematite and TPM). In all analytical and numerical computions, we consider a TEM00 incident gaussian beam mode polarized along x and propagating along z, with an apodization function equals to 1, which corresponds to a flat beam profile at the back aperture of the focusing lens . The profile of the simulated laser beam in water, as presented in [Fig.S4B], agrees well with the experimentally determined one.

2.7 Characterization of the trap stiffness

2.7.1 Experimental determination

We measure the optical force acting on a TPM bead only ($R_{TPM} \approx 0.6$ μm), at equilibrium, by trapping it and measuring the position fluctuations for different powers of the incoming beam. At equilibrium, the restoring force of the optical trap competes with thermal fluctuations, and the stiffness of the trap is given by : $k_{x,y} = k_B T / < \Delta r_{x,y}^2 >$. The probability density function PDF(x,y) is well approximated by a gaussian curve with standard deviation $\sigma_{x,y}^2 =< \Delta r_{x,y}^2 >$ [Fig.S5A]. Fitting the normalized histogram of positions, we extract the stiffness for various intensities, and typically get $k = 0.8 \pm 0.1$ pN/μm at 0.5 mW incident power, with a linear power dependency of the trap stiffness, and a slope of ≈ 1.7 pN/(μm.mW).

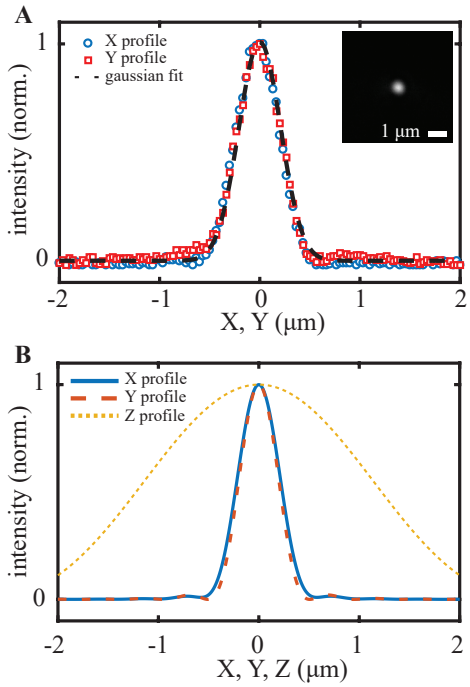

Fig. S4: **Laser beam profile.** **A**. Experimental measurement of the intensity profile at the focus, obtained from the reflection of the laser beam on the glass/water interface, in both the X and Y directions. The dashed line is a fit of the data points with a gaussian function, giving a standard deviation $\sigma = 210$ nm. *Inset :* Image of the reflected laser spot. Scale bar is 1 μm. **B**. Intensity profile in the X, Y, and Z direction for a beam propagating along the Z direction and polarized along X, calculated using the angular spectrum representation of a focused laser beam, at the focus. Fitting with a gaussian the profiles in the transverse plane gives a similar waist as $\sigma = 200$ nm.

2.7.2 Simulations

Following the calculation of the force (see Materials and Methods), we simulate the 1D trajectories of a single spherical TPM particle ($R_T = 500$ nm, $n_T = 1.51$) in water ($n_w = 1.33$), in presence of the focused laser beam. The trapping stiffness is measured as described in the previous section 2.7.1. The results, presented in [Fig.S5B], show good agreement with the experimental values, with a slope of ≈ 2.2 pN/(μm.mW).

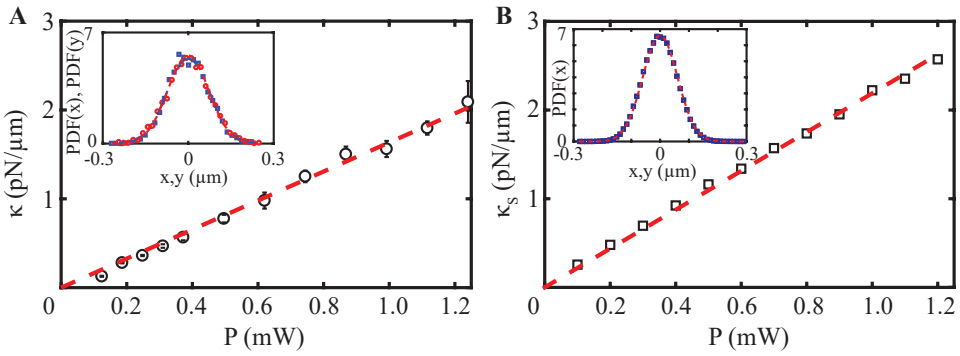

Fig. S5: **Experimental characterization of the trap stiffness for a single TPM bead. A**. Experimental measurement of the stiffness of the trap, determined for various powers of the incoming beam, and fitted by a linear function (red dashed curve), giving a slope of 1.7 pN/(μm.mW). *Inset :* Example of the PDF(x,y) of the position of the bead in the trap at 0.5 mW incident power for both x (blue squares) and y (red circles) coordinates. The PDFs are perfectly fitted by gaussian curves. **B**. Stiffness of the trap extracted from simulated trajectories of trapped $R_T = 500$ nm TPM beads, showing similar trend as experimental data. *Inset :* PDF(x) of the bead at 0.5 mW incident power.

2.8 Optical Forces

In [Fig.S6A,B], we show the 2D mapping of the optical forces for single hematite and TPM beads in water. While the gradient force pulling the particle near the center of the focus dominates for the TPM part, the scattering forces are dominant on the hematite particle, pushed away from the focal region. We further compare the forces and torques acting on individual and individual hematite and TPM particles to the total force exerted on a full heterodimer, using analytical and COMSOL calculations, respectively [Fig.S6C,D]. Summing individual forces, we find a deviation of max. $\sim 10 - 20$ % compared to the case when the full heterodimer is considered. The total force acting on a heterodimer is thus reasonnably approximated by summing the isolated forces of its two components.

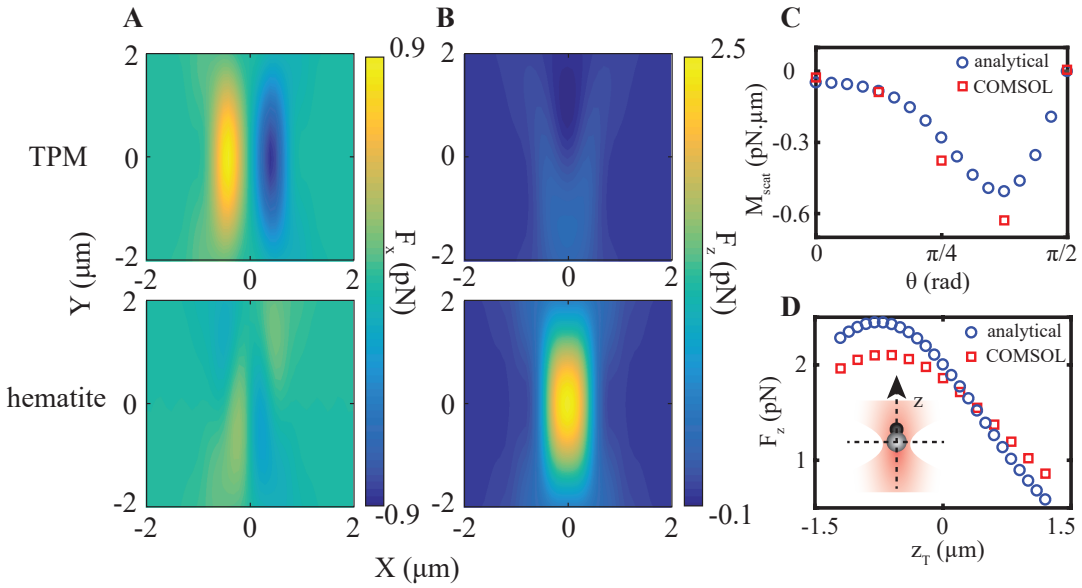

Fig. S6: **Optical forces on the heterodimer. A**. Optical Forces along the X direction for single hematite ($R_H = 250$ nm) and TPM ($R_T = 500$ nm) particles. **B**. Optical Forces along the Z direction. For better comparison, colorbars are identical for both particles. **C**. Computation of the optical torque for a heterodimer with the TPM bead situated at the focus, as a function of the orientation θ. The sum of individual forces on each component in the absence of the other (analytical) is compared to COMSOL calculations considering a full heterodimer. **D**. Similar comparison as in (**C**), but for the force along Z acting on a vertical heterodimer, as a function of the position of the TPM bead. The scheme indicates the considered geometry. All forces and torques are computed for a 1 mW incident power.

2.9 Computation of the phase diagram

We vary both P_{inc} and V_S, and compute the trajectories followed by the heterodimers upon crossing the laser beam at zero noise. For all trajectories, the swimmer starts with the TPM part at $\{x_{T,0} = -1000nm, y_{T,0} = 0, z_{T,0} = 0, \theta_0 = -\pi/8\}$. We assume that stable trapping is achieved as long as the swimmer stays in the focus of the beam, corresponding to $-w_0 < x_T < w0$, and $0 < z_T < z_R$, where w_0 is the waist of the laser, and z_R the Rayleigh range, defined as $z_R = 0.5kw_0^2$, where k is the wavector in water. Crossing is achieved when the swimmer reaches $x_T \geq 2000$ nm, and is ejected when $z_T > z_R$. The equations of the dynamics are

presented in the Material and Methods. All simulated trajectories are performed for 10 s, with a time step of 5 ms.

2.10 Analysis of the angular statistics of swimmers in slender structures, effect of hydrodynamics

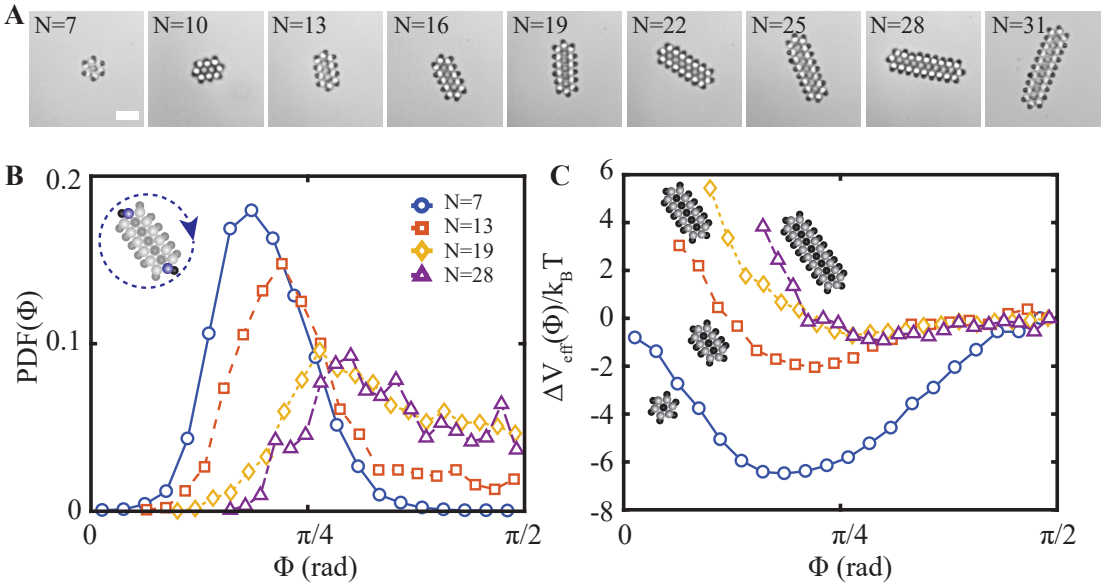

Fig. S7: **Analysis of the orientation of swimmers in slender structures.** **A**. List of slender structures that were investigated, with corresponding number of swimmers N. **B**. Histogram of the orientation Φ of the heterodimers situated at the tips of the structures. Upon increasing the size of the structures, the PDF(Φ) broadens, and the orientation of the heterodimers can flip direction. The scheme for a $N = 19$ structure shows the investigated 'tip swimmers' in blue, together with the sense of rotation (blue arrow). **C**. Corresponding effective potential, shifted so that $V(\pi/2) = 0$. The difference in potential depth is clearly visible, and is less than k_BT for large rods with $N \gtrsim 16$.

The persistence of the motion of an architecture depends on the fluctuations of orientations of the constitutive swimmers. In order to gain insight on the influence of hydrodynamics on the angular distribution of the heterodimers with $n = 3, 4$ neigbors, we investigated the dynamics of slender structures of various lengths, that we use as model systems [Fig.S7]. These rod-like structures exhibit primarily rotational motion around their barycenter, with a rotational speed

dependent on the length of the structure. In addition, in those structures the heterodimers at the tip of the rods have a constant nearest-neighbors environment, independant of the length of the rod-size, and experience a hydrodynamic drag in similar direction. It allows us to investigate the effect of rotation speed of the machine on the orientational dynamics of the heterodimers with $n = 3, 4$ at the tip, and quantify the effect of hydrodynamics. We study the dynamics of elongated rods ranging from $N = 7$ to $N = 31$ swimmers [Fig.S7A]. The results, presented in [Fig.S7B], show a broadening of the angular distribution for increasing rod size and subsequent decreasing rotational velocity. It highlights the role of hydrodynamics on the orientational dynamics of the swimmers, coupled to collective motion of the metamachine. We estimate an effective hydrodynamic potential from the distribution of angles, assuming that Boltzmann statistics remain valid, a questionable choice out of equilibrium but allowing us to get a physical intuition of the strength of the effect. We obtain an effective potential $V(\Phi)/k_BT \approx -\ln PDF(\Phi)$ [Fig.S7C], and presenting a well defined minimum $\sim 6k_BT$ for 7-swimmers rods, vanishing to $\sim 1k_BT$ for rods larger than ~ 16 swimmers. It highlights the "stabilization" effect of hydrodynamics in the orientational dynamics of the heterodimers pushing on the edge. As a result, large and slow structures are more likely to be dynamically metastable, and switch between different dynamics.

References and Notes

1. Howse, J. R. *et al.* Self-motile colloidal particles: From directed propulsion to random walk. *Phys. Rev. Lett.* **99**, 048102 (2007).

2. Aubret, A., Ramananarivo, S. & Palacci, J. Eppur si muove, and yet it moves: Patchy (phoretic) swimmers. *Current Opinion in Colloid & Interface Science* **30**, 81 – 89 (2017).

3. van der Wel, C. *et al.* Preparation of colloidal organosilica spheres through spontaneous emulsification. *Langmuir : the ACS journal of surfaces and colloids* **33**, 8174–8180 (2017).

4. Novotny, L. & Hecht, B. *Principles of Nano-Optics* (Cambridge University Press, 2006).